JPE 19-6-6

https://doi.org/10.6113/JPE.2019.19.6.1403
ISSN(Print): 1598-2092 / ISSN(Online): 2093-4718

# Sliding Mode Controller Applied to Coupled Inductor Dual Boost Inverters

Yu Fang†, Songyin Cao*, and Pat Wheeler**

†,*College of Information Engineering, Yangzhou University, Yangzhou, China
**Department of Electrical and Electronic Engineering, University of Nottingham, Nottingham, ENG, UK

**Abstract**

A coupled inductor-dual boost-inverter (CIDBI) with a differential structure has been presented for application to a micro-inverter photovoltaic module system due to its turn ratio of a high-voltage level. However, it is difficult to design a CIDBI converter with a conventional PI regulator to be stable and achieve good dynamic performance, given the fact that it is a high order system. In view of this situation, a sliding mode control (SMC) strategy is introduced in this paper, and two different sliding mode controllers (SMCs) are proposed and adopted in the left and right side of two Boost sub-circuits to implement the corresponding regulation of the voltage and current. The schemes of the SMCs have been elaborated in this paper including the establishment of a system variable structure model, selection of the sliding surface, determination of the control law, and presentation of the reaching conditions and sliding domain. Finally, the mathematic analysis and the proposed SMC are verified by experimental results.

**Key words:** Coupled inductor, Micro inverter, Photovoltaic (PV) power generation, Sliding mode control

## I. INTRODUCTION

A grid-connected micro-inverter is an effective way to solve the hot spot effects of photovoltaic modules and to improve the efficiency of photovoltaic power generation. There are two main grid-connected power generation methods for low-voltage photovoltaic modules. 1) Single-stage inverters connected to a grid by the line transformer boost mode. 2) Two-stage inverter consisting of a front-stage DC-DC boost circuit and a back-stage inverter. In the first method, when the voltage of a photovoltaic module is low, the turn ratio of the line transformer is large. Hence, the power loss of transformer is large. In the second method, a two-stage circuit is adopted, and the conversion efficiency of the system is not high. It can be seen that these two methods are not conducive to the efficient generation of small and medium power from photovoltaic cells to the grid.

The CIDBI proposed in [1] can meet the voltage boost requirements of photovoltaic modules and AC grid-connected. In other words, it is able to realize one-stage transformerless grid-connected.

The differential CIDBI presented in [1] and shown in Fig. 1 is composed of two coupled inductor boost circuits that generate an ac output voltage that is larger than the dc input. It depends on the instantaneous duty cycle and turn ratio of the coupled inductor, and uses only one power processing stage. Fig. 1 shows that there is one DC source $B_1$. It can be seen that $L_1$ and $L_2$ commonly share the same magnetic core, while $L_3$ and $L_4$ use another. Thus, the coupled inductors are constructed. One boost circuit consists of $L_1$, $L_2$ and $C_2$, the switches $T_1$ and $T_2$, and their body diodes $D_1$ and $D_2$. The other boost circuit consists of $L_3$, $L_4$ and $C_3$, the switches $T_3$ and $T_4$, and their body diodes $D_3$ and $D_4$. It is clear that the right-side circuit and the left side circuit represent boost converters with a coupled inductor. In [1], a CIDBI can be employed as micro inverter integrated with a much lower voltage PV array and achieve a high energy conversion efficiency due to its one-stage boost circuit architecture. However, it is difficult to achieve a tradeoff between the stability and the fast dynamic response of a CIDBI by using traditional linear controllers. This results in energy loss due to sudden changes in photovoltaic applications.

Manuscript received Apr. 14, 2019; accepted Jun. 27, 2019
Recommended for publication by Associate Editor Fuxin Liu.
†Corresponding Author: yfang@yzu.edu.cn
Tel: +86-514-87978319, Fax: +86-514-87971865, Yangzhou University
*College of Information Engineering, Yangzhou University, China
**Dept. of Electrical & Electron. Eng., The Univ. of Nottingham, UK

© 2019 KIPE

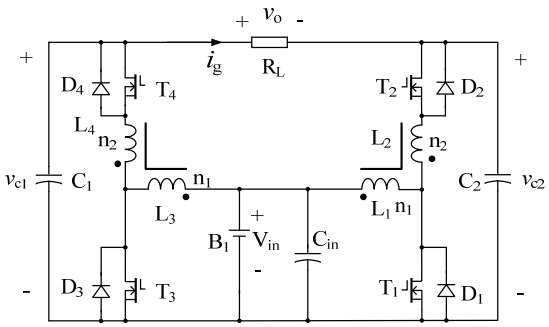


Fig. 1. Main circuit of CIDBI.

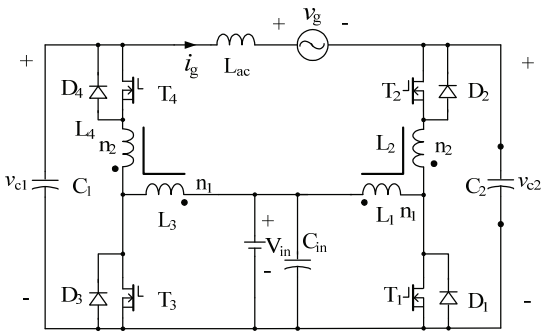


Fig. 2. Main circuit of the CIDBI after the insertion of $L_{ac}$.

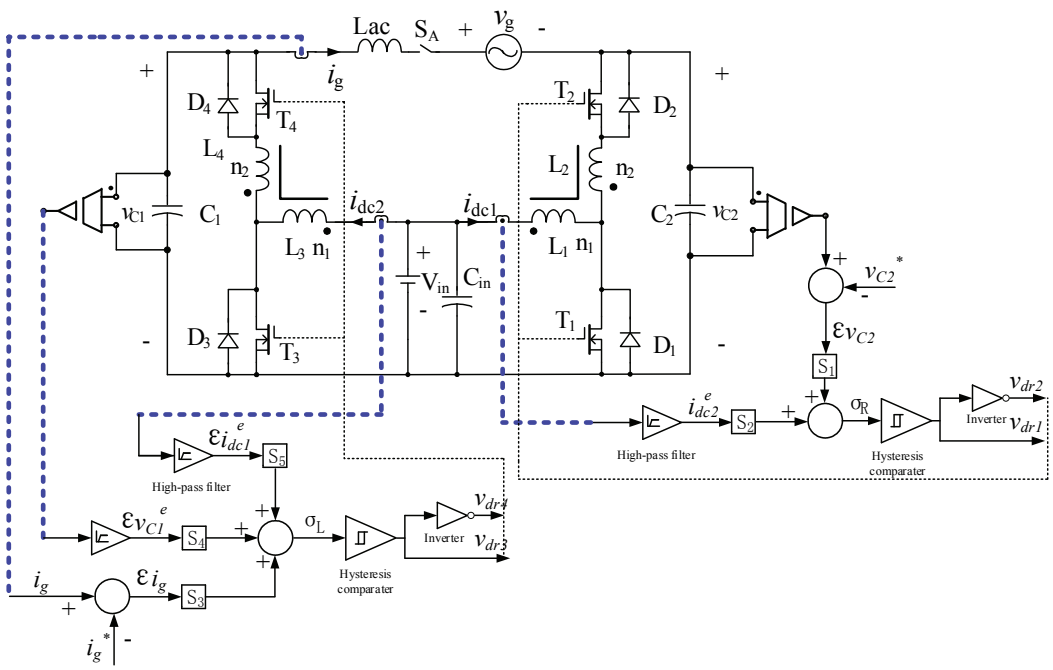


Fig. 3. Schematic diagram of a CIDBI with two sliding mode controllers.

In order to obtain a smoother grid current $i_g$, an AC output inductor $L_{ac}$ is added on the basis of Fig. 1, as shown in Fig. 2. Thus, the current $i_g$ through $L_{ac}$ is shaped by adapting the voltage difference ($v_{c1}$-$v_{c2}$). In this paper, two different sliding mode controllers are proposed and adopted in the left and right side circuit of the CIDBI to realize grid-connected power generation. In addition, the SMCs for grid-connected power generation are discussed and analyzed. As a result, the energy of low-voltage photovoltaic modules can be transferred into a power grid by a CIDBI with good performance.

## II. Analysis and Design of SMCs

The main circuit diagram of a CIDBI shown in the Fig. 2 can be divided into two subsystems that are controlled by different sliding modes, as shown in Fig. 3. In order to generate an ac output current $i_g$ from dc sources, the left-side circuit is controlled to shape the grid current $i_g$, and the right-side circuit is controlled to make the output voltage stable, which is close to $v_{C2}$* (reference voltage). These two parts of the controller can realize decoupling control. Next, error state equations of the left circuit and right circuit are deduced.

### A. Right-Side Circuit

The CIDBI is based on a boost converter. Hence, the voltage $v_{C2}$ must never fall below $V_{in}$. That is to say, the output voltage is a dc-biased sinusoidal voltage as presented in equation (1). In addition, equation (1) defines the reference for $v_{C2}$.

$$v_{c2}^*(t) = V_m^* \sin(\omega t + \pi) + V_{dc}^* \tag{1}$$

Assume the grid voltage is as follows

$$v_g(t) = V_g \sin(\omega t) \tag{2}$$

When in steady operation, the grid current should follow the reference current $i_g^*$. Here it is assumed that the reference grid current and the grid current are as follows:

$$i_g^*(t) = I_g^* \sin(\omega t) \tag{3}$$

$$i_g(t) = I_g \sin(\omega t) \tag{4}$$

Since the differential output is constructed by the left-side circuit and right-side circuit, the reference ac voltage component is given as follows:

$$V_m^* = V_g / 2 \tag{5}$$

In order to keep the voltage $v_{c2}$ higher than $V_{in}$ all the time, the following inequality is met.

$$V_{dc}^* > V_{dc} + V_g / 2 \tag{6}$$

$v_{C2}^*$can be achieved by controlling $T_1$ and $T_2$ in the right-side boost circuit, and the pulse control signals $v_{dr1}$ and $v_{dr2}$ should be complementary. In light of the switching states, the right side of the converter can be equivalent to two sub-circuits as shown in Fig. 4. In addition, the left side of the CIDBI can be considered as the current source. Thus, the calculation formula of the duty cycle ratio $d_R(t)$ for the right side is as follows.

$$d_R(t) = \frac{v_{c2}^*(t) - V_{in}}{v_{c2}^*(t) + N \cdot V_{in}} = \frac{V_m^* \sin(\omega t + \pi) + V_{dc}^* - V_{in}}{V_m^* \sin(\omega t + \pi) + V_{dc}^* + N \cdot V_{in}} \tag{7}$$

Where, N is the turn ratio of the coupled inductor (seen in the Fig. 1: $n_2/n_1$).

The average power of the output should be equal to that of the input according to the instantaneous power theory. Thus, equation (8) can be obtained as follows.

$$V_{in} \cdot i_{dc1}^*(t) = C_2 \cdot v_{c2}^*(t) \cdot \frac{d(v_{c2}^*(t))}{dt} - v_{c2}^*(t) i_g^*(t) \tag{8}$$

Substituting expressions (1), (2), (4) and (5) into equation (8), the reference value $i_{dc1}$* for the dc input current can be expressed as (9).

$$i_{dc1}^*(t) = \frac{1}{V_{in}} \begin{bmatrix} \frac{1}{2} V_m^* \cdot I_g^* (1 - \cos(2\omega t)) - V_{dc}^* \cdot I_g^* \sin(\omega t) \\ -\omega C_2 \cdot (V_{dc}^* \cdot V_m^* \cos(\omega t) - \frac{1}{2} (V_m^*)^2 \sin(2\omega t)) \end{bmatrix} \tag{9}$$

Expression (9) describes the average input current $i_{dc1}$ through the coupled inductor $L_1/L_2$. In fact, the input current contains a high-frequency ripple current that can be neglected since it has no effect on the effective value of the current.

The switching function can be defined in expression (10), where, $\gamma$ is the state variable.

$$\gamma = \begin{cases} 1 & \text{When } T_1 \text{ is ON and } T_2(D_2) \text{ off} \\ 0 & \text{When } T_1 \text{ is OFF and } T_2(D_2) \text{ on} \end{cases} \tag{10}$$

It is clear that the corresponding output energy increases when $\gamma$=1. In this state, the inductor $L_1$ and the output capacitance $C_2$ are decoupled and the current through $L_1$ is increased linearly, i.e. the energy storage. In addition, $i_g$ flows to $C_2$ as shown in the Fig. 4(a). When $\gamma$=0, the energy is transferred to $C_2$ by the coupled inductor $L_1/L_2$ as shown in the Fig. 4(b).

It can be seen from Fig. 4 that there are two error variables that are defined as $\varepsilon v_{C2}$ for the output capacitance voltage, and

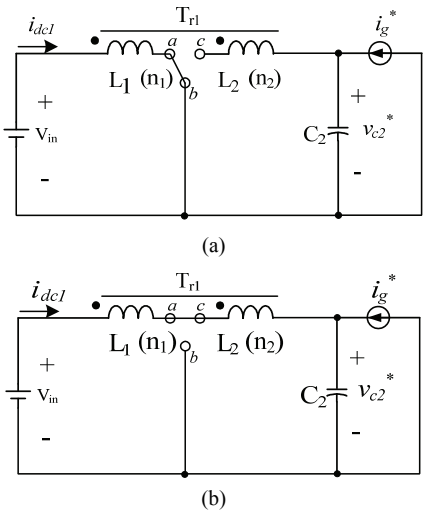


Fig. 4. Two structures of the right-side converter. (a) $T_1$ is on and $T_2(D_2)$ off. (b) $T_2(D_2)$ is on and $T_1$ off.

$\varepsilon i_{dc1}$ for the coupled inductor current in expression (11).

$$\begin{cases} \varepsilon v_{C2} = v_{C2} - v_{C2}^* \\ \varepsilon i_{dc1} = i_{dc1} - i_{dc1}^* \end{cases} \tag{11}$$

As a result, the state error equation of the right-side converter can be written as (12).

$$\dot{x} = Ax + B\gamma + D \tag{12}$$

Where:

$$x = [\varepsilon v_{C2}, \varepsilon i_{dc1}]^T \tag{13}$$

$$A = \begin{bmatrix} 0 & \frac{1}{C_2} \\ -\frac{1}{L_1 \cdot (1+N)} & 0 \end{bmatrix} \tag{14}$$

$$B = \begin{bmatrix} -\frac{i_{dc1}}{C_2} \\ \frac{v_{c2} + N \cdot V_{in}}{L_1 \cdot (1+N)} \end{bmatrix} \tag{15}$$

$$D = \begin{bmatrix} \frac{i_g^* + i_{dc1}^*}{C_2} \\ \frac{V_{in} - v_{c2}^*}{L_1 \cdot (1+N)} \end{bmatrix} \tag{16}$$

It is noted that the low-frequency reference functions, when compared with the switching frequency, can be considered as quasistatic, in such a way that the term of the derived function for the reference is generally neglected in equation (12).

### *B. Left-Side Circuit*

The left-side subsystem is seen as the current source and controlled to shape the grid current. Actually, the voltage of $L_{ac}$ can be regulated only if the voltage $v_{C1}$ across $C_1$ is controlled. As a result, the grid current $i_g$ is obtained.

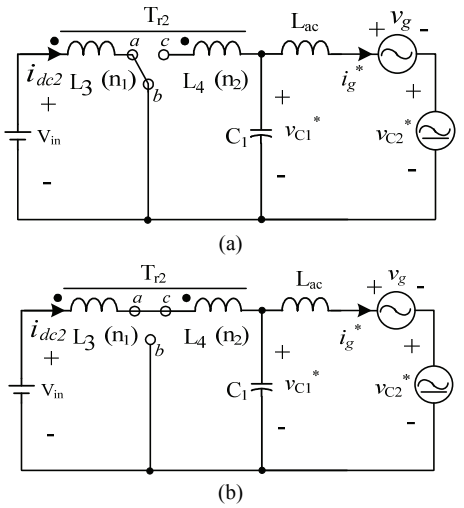


Fig. 5. Two structures of the left-side converter: (a) $T_3$ is on and $T_4(D_4)$ off; (b) $T_4(D_4)$ is on and $T_3$ off.

Additionally, since the inductor $L_{ac}$ is designed to filer the high-frequency switching ripple, its steady-state low-frequency voltage is small. In addition, the voltage $v_{C1}$ should be close to ($v_{C2}$+$v_g$). Thus, $v_{C1}$ can be expressed as (17).

$$v_{C1}^{*}(t) \approx V_m^{*}\sin(\omega t) + V_{dc}^{*} \tag{17}$$

The ac component of expression (17) is complementary to that of the expression (1). Thus, the phase difference is 180°. In addition, the equations of duty cycle ratio $d_L(t)$ and $i_{dc2}^{*}$ are similar to (7) and (9), with $\pi$ rad added to the arguments of the sine or cosine function (or simply the terms in sin(ωt) and cos(ωt) change their signs, while the terms involving 2ωt remain unchanged).

In order to follow $i_g^{*}$, the switches $T_3$ and $T_4$ in the left-side converter are controlled with a certain duty cycle ratio $d_L$, and their pulse control signals $v_{dr3}$ and $v_{dr4}$ should be complementary to each other. In light of the switching state, the left-side converter can be equivalent to two sub circuits as shown in Fig. 5, and the right-side converter is taken as the voltage source in Fig. 5.

The two states in Fig. 5 can be described by the switching function as (18).

$$\lambda = \begin{cases} 1 & \text{When } T_3 \text{ is on and } T_4(D_4) \text{ off} \\ 0 & \text{When } T_3 \text{ is off and } T_4(D_4) \text{ on} \end{cases} \tag{18}$$

Assuming that the error variable for the filter $L_{ac}$ is $\varepsilon i_g$, the error variable for the filter $C_1$ is $\varepsilon v_{C1}$, and the error variable for the coupled inductor$L_3/L_4$ is $\varepsilon i_{dc2}$. This is shown in expression (19).

$$\begin{cases} \varepsilon i_g = i_g - i_g^{*} \\ \varepsilon v_{C1} = v_{C1} - v_{C1}^{*} \\ \varepsilon i_{dc2} = i_{dc2} - i_{dc2}^{*} \end{cases} \tag{19}$$

After defining the error variables, the state error equation (20) can be written.

$$\dot{y} = A' y + B'\lambda + D' \tag{20}$$

Where:

$$y = [\varepsilon i_g, \varepsilon v_{C1}, \varepsilon i_{dc2}]^{T} \tag{21}$$

$$A' = \begin{bmatrix} 0 & \frac{1}{L_{ac}} & 0 \\ -\frac{1}{C_1} & 0 & \frac{1}{C_1} \\ 0 & -\frac{1}{L_3\cdot(1+N)} & 0 \end{bmatrix} \tag{22}$$

$$B' = \begin{bmatrix} 0 \\ -\frac{i_{dc2}}{C_1} \\ \frac{v_{C1} + N\cdot V_{in}}{L_3\cdot(1+N)} \end{bmatrix} \tag{23}$$

$$D' = \begin{bmatrix} \frac{v_{C1}^{*} - v_{C2}^{*} - V_g}{L_{ac}} \\ \frac{i_{dc2}^{*} - i_g^{*}}{C_1} \\ \frac{V_{in} - v_{C1}^{*}}{L_3\cdot(1+N)} \end{bmatrix} \tag{24}$$

The derived function for the reference is neglected in the state error equation (20) as in the previous section. Through the above analysis, the error state equation of the CIDBI is obtained.

## III. Control Strategy

Sliding mode control can change the circuit structure by controlling the switch state. The sliding mode method is implemented in the error state space, and the trajectory through the spatial origin (the desired stable state) is well designed. When the representative point reaches the trajectory, approaches it, and then reaches the origin, zero error is achieved [10]-[16]. Such a trajectory is called a sliding surface (σ), and this motion is called a sliding mode or a sliding mode method. The designed sliding surface space is divided into two subspaces, each of which is associated with a structure. The motion in the vicinity of the sliding surface must point to the sliding surface [17]-[24]. This is a necessary and sufficient condition for the existence of the sliding surface, which is expressed mathematically as follows:

$$\begin{cases} \dot{\sigma} < 0, \text{When } \sigma > 0 \\ \dot{\sigma} > 0, \text{When } \sigma < 0 \end{cases} \tag{25}$$

Considering the fact that actual switching devices are difficult to operate at infinitely high switching frequencies, the actual sliding mode is not always on the sliding surface, and the quasi-sliding mode is usually used to achieve control [25]-[27].

*A. Implementation of the Right-Side SMC*

The sliding mode surface $\sigma_R$ is defined by expression (26), which can be considered as the weight of the error. If $S_1$ and $S_2$ are taken to be constant, the sliding mode surface is a straight line on the plane of $\varepsilon_{v_{C2}} \times \varepsilon_{i_{dc1}}$, and the slope is decided by $\alpha_R=S_1/S_2$. In expression (25), the units: $S_2$ is ohms; $S_1$ is dimensionless; and $\alpha_R$ is Siemens.

$$\sigma_R = S_1 \cdot \varepsilon_{v_{C2}} + S_2 \cdot \varepsilon_{i_{dc1}} \tag{26}$$

Assuming that $S=[S_1, S_2]^T$, expression (25) can be expressed by (27).

$$\sigma_R = S^T x \tag{27}$$

Since the error variables are defined by (12), if the representative point is below the surface $\sigma_R$, the energy of the capacitor $C_2$ and the inductor $L_1$ is reduced. Then $\gamma$ should be set to 1, whereas $\gamma$ should be set to 0 when it is above $\sigma_R$. Thus, expression (28) can be obtained.

$$\gamma = \begin{cases} 1 & \text{When } \sigma_R < 0 \\ 0 & \text{When } \sigma_R > 0 \end{cases} \tag{28}$$

Since the error variables are very small and approach zero by comparison with the reference values, the existing condition (25) for the sliding mode surface on the right side can be written by (29) and (30).

$$\dot{\sigma}_R = S^T D < 0, \quad \sigma_R > 0 \tag{29}$$

$$\dot{\sigma}_R = S^T B + S^T D > 0, \quad \sigma_R < 0 \tag{30}$$

Substituting matrixes B and D into (29) and (30), the expression (31) and (32) can be obtained.

$$S_1 \cdot \frac{i_g^* + i_{dc1}^*}{C_2} + S_2 \cdot \frac{V_{in} - v_{C2}^*}{L_1 \cdot (1+N)} < 0 \tag{31}$$

$$S_1 \cdot \frac{i_g^* + i_{dc1}^* - i_{dc1}}{C_2} + S_2 \cdot \frac{v_{C2} - v_{C2}^* + (1+N) \cdot V_{in}}{L_1 \cdot (1+N)} > 0 \tag{32}$$

It can be concluded from (31) and (32) that $S_1$ and $S_2$ choose non-negative values if the sliding mode surface exists as presented in (26).

If the actual system adopts the fixed hysteresis width of 2δ in Fig. 6, the control rules can be rewritten into (33). In addition, the phase plane trajectory oscillates on both sides of the sliding mode surface ($\sigma_R=0$), as shown in Fig. 7.

$$\gamma = \begin{cases} 1 & \text{When } \sigma_R < -\delta \text{ or } (\dot{\sigma}_R > 0 \text{ and } |\sigma_R| < \delta) \\ 0 & \text{When } \sigma_R > +\delta \text{ or } (\dot{\sigma}_R < 0 \text{ and } |\sigma_R| < \delta) \end{cases} \tag{33}$$

It can be seen from Fig. 7 that $\sigma_R$ must increase from –δ to +δ during $\Delta t_1$ ($\dot{\sigma}_R > 0$), while $\sigma_R$ must decrease from +δ to -δ during $\Delta t_2$ ($\dot{\sigma}_R < 0$). Assuming that the state trajectory remains the same near $\sigma_R=0$, formula (34) for the switching frequency can be deduced from Fig. 7.

$$f_s = 1 \Big/ (\Delta t_1 + \Delta t_2) \tag{34}$$

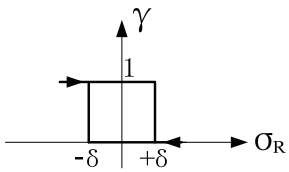


Fig. 6. Switching function γ.

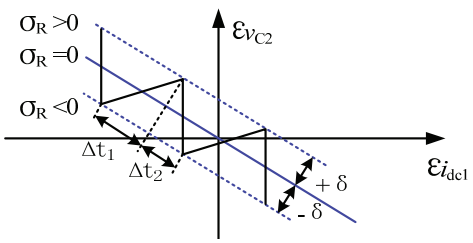


Fig. 7. Waveform of $\sigma_R$.

Where, $\Delta t_1$ corresponds to the switching state $\gamma=1$, and $\Delta t_2$ corresponds to $\gamma=0$. In addition, $\Delta t_1$ and $\Delta t_2$ can be solved by (35) and (36), respectively.

$$\Delta t_1 = \frac{2\delta}{\left( S_1 \cdot \frac{i_g^* + i_{dc1}^* - i_{dc1}}{C_2} + S_2 \cdot \frac{v_{C2} - v_{C2}^* + (1+N) \cdot V_{in}}{L_1 \cdot (1+N)} \right)} \tag{35}$$

$$\Delta t_2 = \frac{-2\delta}{\left( S_1 \cdot \frac{i_g^* + i_{dc1}^*}{C_2} + S_2 \cdot \frac{V_{in} - v_{C2}^*}{L_1 \cdot (1+N)} \right)} \tag{36}$$

Substituting (35) and (36) into (34), the maximum switching frequency can be obtained as (37) at the positive peak value of $v_{C2}$, assuming $i_g^*=0$ and the corresponding $i_{dc1}^*=0$ in the state of a light load.

$$f_{smax} = \frac{S_2 \cdot V_{in}}{L_1 \cdot 2\delta} \cdot \frac{v_{C2}^* - V_{in}}{v_{C2}^* + N \cdot V_{in}} \tag{37}$$

The duty cycle ratio is defined as follows:

$$d_R(t) = \frac{\Delta t_1}{\Delta t_1 + \Delta t_2} \tag{38}$$

Substituting (34) and (35) into (38), the steady switching frequency can be obtained as (39), depending on steady operation points such as the duty cycle, control parameters and value of the grid current.

$$f_{SR}(t) = \left[ d_R(t) / (2\delta) \right] \cdot \left[ S_2 \cdot V_{in} / L_1 + S_1 \cdot i_g^*(t) / C_2 \right] \tag{39}$$

When $i_g$ reaches a negative peak value, the variations of $i_{dc1}$ and $v_{C2}$ are the largest. At this time, the duty cycle is the largest and the switching frequency the highest. As a result, $L_1$ and $C_2$ can be designed as (40) in order to ensure that all of the magnetic components are unsaturated within the scope of the switching frequency.

$$L_1(t) \geq \frac{V_{in} \cdot d_{R\max}}{\Delta I_{dc1\max} \cdot f_{SR\min}} \quad \textit{and} \quad C_2 \geq \frac{I_g^* \cdot d_{R\max}}{\Delta V_{C2\max} \cdot f_{SR\min}} \tag{40}$$

*B. Implementation of the Left-Side SMC*

Since the left side is a third order system, the sliding mode surface $\sigma_L$ can be obtained by (41).

$$\sigma_L = S_3 \cdot \varepsilon i_g + S_4 \cdot \varepsilon v_{C1} + S_5 \cdot \varepsilon i_{dc2} \tag{41}$$

Let $S_L=[S_3, S_4, S_5]^T$, and expression (41) can be written as (42).

$$\sigma_L = S_L{}^T y \tag{42}$$

Since the error variables are defined by (19), if the representative point is below the surface $\sigma_L$, the energy of the capacitor $C_1$ and the inductor $L_3$ is reduced. Then $\lambda$ should be set to 1, whereas $\lambda$ should be set to 0 when it is above $\sigma_L$. Thus, expression (43) can be obtained.

$$\lambda = \begin{cases} 1 \ \text{When} \ \sigma_L < 0 \\ 0 \ \text{When} \ \sigma_L > 0 \end{cases} \tag{43}$$

Since the error variable is very small and approaches zero by a comparison with the reference values, the existing condition (25) for the sliding mode surface on the left side can be written by (44) and (45).

$$\dot{\sigma}_L = S^T D' < 0, \ \ \sigma_L > 0 \tag{44}$$

$$\dot{\sigma}_L = S_L{}^T B' + S_L{}^T D' > 0, \ \ \sigma_L < 0 \tag{45}$$

Substituting matrixes $B'$ and $D'$ into (44) and (45), the expression (46) and (47) can be obtained.

$$S_3 \frac{v_{C1}{}^* - v_{C2}{}^* - V_g}{L_{ac}} + S_4 \frac{i_{dc2}{}^* - i_g{}^*}{C_1} + S_5 \frac{V_{in} - v_{C1}{}^*}{L_3 \cdot (1+N)} < 0 \tag{46}$$

$$S_3 \frac{v_{C1}{}^* - v_{C2}{}^* - V_g}{L_{ac}} + S_4 \frac{i_{dc2}{}^* - i_{dc2} - i_g{}^*}{C_1} + S_5 \frac{V_{in}(1+N) + v_{C1} - v_{C1}{}^*}{L_3 \cdot (1+N)} > 0 \tag{47}$$

If expressions (46) and (47) are established, the existing condition for the sliding mode is met. In addition, the sufficient condition for the existence of the sliding mode surface defined by (41) is that $S_3$, $S_4$ and $S_5$ choose nonnegative values.

Just like the right side, the hysteresis comparison control is employed to avoid an excessive switching frequency. Here, assuming that the hysteresis width is $2\zeta$, the phase plane trajectory oscillates on both sides of the sliding mode surface ($\sigma_L=0$).

Defining the on time of switch $T_3$ for $\Delta t_1$, which corresponds to the switching state $\lambda=1$; and the off time for $\Delta t_2$, which corresponds to the switching state $\lambda=0$; $\Delta t_1$ and $\Delta t_2$ can be solved by (48) and (49), respectively.

$$\Delta t_1 = \frac{2\xi}{\left( S_3 \frac{v_{C1}{}^* - v_{C2}{}^* - V_g}{L_{ac}} + S_4 \cdot \frac{i_{dc2}{}^* - i_{dc2} - i_g{}^*}{C_1} + S_5 \cdot \frac{V_{in}(1+N) + v_{C1} - v_{C1}{}^*}{L_3 \cdot (1+N)} \right)} \tag{48}$$

$$\Delta t_2 = \frac{-2\xi}{\left( S_3 \frac{v_{C1}{}^* - v_{C2}{}^* - V_g}{L_{ac}} + S_4 \frac{i_{dc2}{}^* - i_g{}^*}{C_1} + S_5 \frac{V_{in} - v_{C1}{}^*}{L_3 \cdot (1+N)} \right)} \tag{49}$$

The same as the right-side converter, the maximum switching frequency occurs at a light load. Assuming $i_g{}^*=0$ and the corresponding $i_{dc2}{}^*=0$, and noticing that the coefficient of the term of $S_3$ is zero and that the terms of $S_4$ and $S_5$ are like (35) and (36), expression (50) can be obtained.

$$f_{smax} = \frac{S_4 \cdot V_{in}}{L_3 \cdot 2\zeta} \cdot \frac{v_{C1}{}^* - V_{in}}{v_{C1}{}^* + N \cdot V_{in}} \tag{50}$$

It can be seen that the last two terms are the same with the right side in the existing conditions (46) and (47) for the sliding mode surface of the left-side converter, i.e. $S_4=S_1$ and $S_5=S_2$. Therefore, only the value of $S_3$ needs to be confirmed. Since the CIDBI is used for grid connected power generation, $v_{C1}{}^* - v_{C2}{}^* - V_g > 0$ in (46) must be established, and this difference value should be equal to $v_{Lac}$ of $L_{ac}$, which result in $S_3>0$. As a result, the upper limit of $S_3$ can be solved by (46) under the condition of the maximum of $\left| v_{Lac} \right|$.

The steady state switching frequency can be solved by (51) only if $\Delta t_1+\Delta t_2$ is calculated during the period of hysteresis, which is like the right side.

$$f_{SL}(t) = \left[ d_L(t) / (2\zeta) \right] \cdot \left[ S_5 \cdot V_{in} / L_3 - S_4 \cdot i_g{}^*(t) / C_1 \right] \tag{51}$$

When $i_g$ reaches the positive peak value, variations of $i_{dc2}$ and $v_{C1}$ are the largest. Hence, the values of $L_3$ and $C_1$ can be chosen by (52).

$$L_3(t) \geq \frac{V_{in} \cdot d_{L\max}}{\Delta I_{dc2\max} \cdot f_{SL\min}} \ \ and \ \ C_1 \geq \frac{I_g{}^* \cdot d_{L\max}}{\Delta V_{C2\max} \cdot f_{SL\min}} \tag{52}$$

Such a high-pass filter is suitable for cases where the reference of an indirect variable is calculated. The controller tries to offset the sum of the weights of the errors after controlling the power circuit, not just an error. In this way, if one of these references is wrong, it leads to tracing defects. This technology is highly suitable for DC-DC converters. In current applications, the formation of low-frequency AC (twice the grid frequency) is considered to be quasi-static. Therefore, the derivatives of these quasi-static variables can be considered to be zero. In the feedback, the low-frequency components are filtered by a high-pass filter. Thus, it can be considered that the low-frequency components have tracked the reference value in the steady state, and only high-frequency components and the spike need to be regulated.

Thus, it is feasible to collect indirect variables with high-pass filters. Of course, the introduction of high-pass filters increases the order of the system. Generally speaking, the transient response of a system is easier to oscillate than that of the case where the indirect variables have references. The

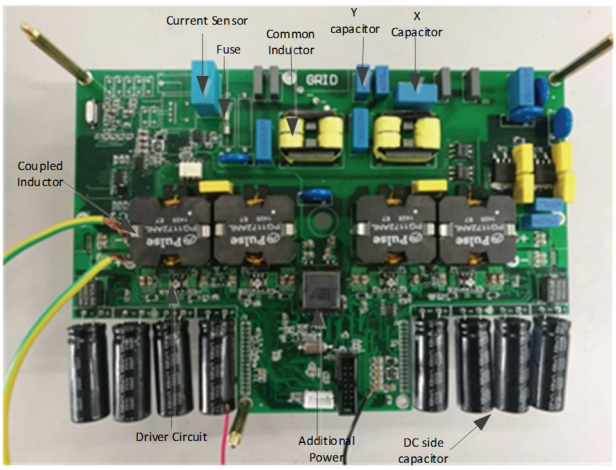


Fig. 8. Experimental prototype of photovoltaic grid-connected micro-inverters based on the CIDBI.

TABLE I
PROTOTYPE SPECIFICATIONS

| | |
|---|---|
| Output power: Po | 480W |
| Grid maximum voltage: $v_g$ | 230Vrms |
| MPP voltage: $V_{in}$ | 35V |
| Grid frequency: $f_0$ | 50Hz |
| Maximum switching frequency: $f_{smax}$ | 130kHz |

cut-off frequency of a high-pass filter should be set high enough that it has little effect on the dynamic performance of the circuit. On the other hand, high-pass filters should be sensitive to the resonant points of $L_1$, $C_1$, or $L_2$, $C_2$. It should be noted that the resonant frequency of a switching circuit also depends on the duty cycle ratio. Because the filter system is insensitive to current detection when the switch is on for a long time (especially when starting), the inductance current should be limited for the sake of safety.

In addition, the selection of $L_{ac}$ should also consider the resonant frequency of the high-pass filter. In particular, the design of the $v_{C1}$ high-pass filter should take full account of the resonant frequency of $L_{ac}$, $C_1$ and $C_2$. In addition, when starting, the DC voltage on $v_{C2}$ needs to be established first. Then the grid-connected relay closes, and slowly increases the grid-connected current.

## IV. DESIGN EXAMPLE AND EXPERIMENTAL RESULTS

In order to verify the correctness of the above theoretical analysis, a two-channel experimental prototype has been built as shown in Fig. 8. In the prototype, each channel is connected to a photovoltaic module. The performance parameters of only one channel are given here. The input dc source is a PV array whose open voltage is 44V and the maximum power point (MPP) voltage is 35V. The prototype specifications are listed in Table I.

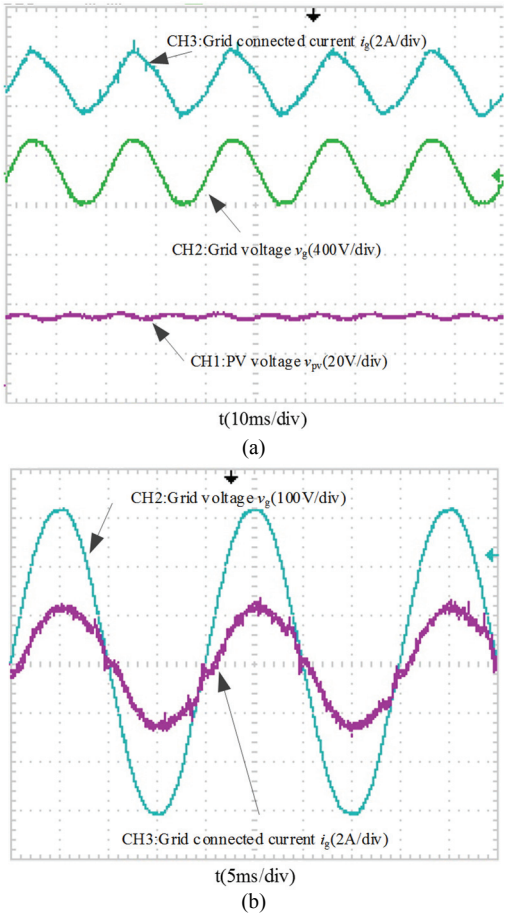


Fig. 9. Main steady operation waveforms of grid-connected generation with the: (a) PI controller in reference [1], (b) SMC in this paper.

In order to regulate the grid current $i_g$ linearly with the duty cycle ranging from 0.3 to 0.75, the dc bias voltage $V_{dc}$ is chosen to be 280V, and the turn ratio of the coupled inductor is 4. Assuming that the grid current is 1.43Arms at the MPP, the reference current and voltage are as follows.

$$\begin{cases} i_g^*(t) = 1.43\sin(\omega t) \\ v_{C2}^*(t) = 162.6\sin(\omega t + \pi) + 280 \end{cases} \tag{53}$$

It is clear that $V_{C2max}$=442.6V.

The DC capacitor $C_1$ is 6×2200$\mu$F; $T_1$ and $T_3$ are IPB072N15N3G from Infineon (150V/93A @100°C), Rdson =7.2mΩ; and $T_2$ and $T_4$ are SPB17N80C3 from Infineon (800V/17A @100°). Main experimental waveforms are given in Fig. 9. Here, $v_g$ is the utility grid voltage, $i_g$ is the grid connected current, and $v_{pv}$ is the PV voltage. Fig. 9(a) shows steady operation waveforms with the PI controller in [1], and Fig. 9(b) presents waveforms based on the SMC in this paper. The grid connected current waveform $i_g$(CH3) in Fig. 9(b) is clearly much better than that in Fig. 9(a). When the output power reaches 221W, the efficiency of the CIDBI is greater than 95.8%, the total harmonic distortion of $i_g$ is equal to 1.52%, and the power factor is not less than 0.99. It is clear

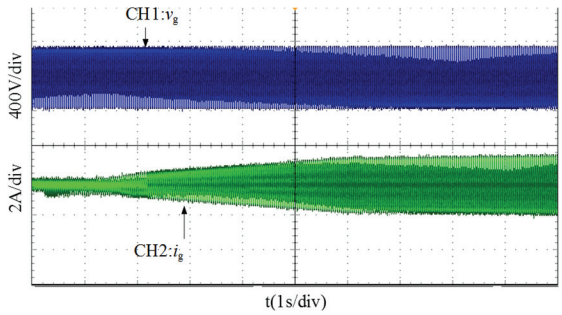


Fig. 10. Start-up generation waveform of a micro inverter.

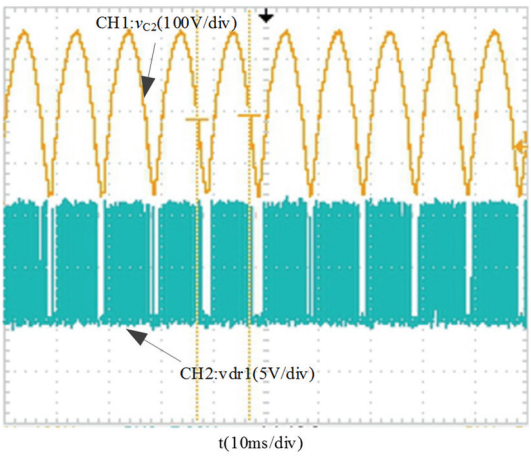


Fig. 11. Driving waveform of $T_1$ and the voltage on $C_2$ in the right-side circuit.

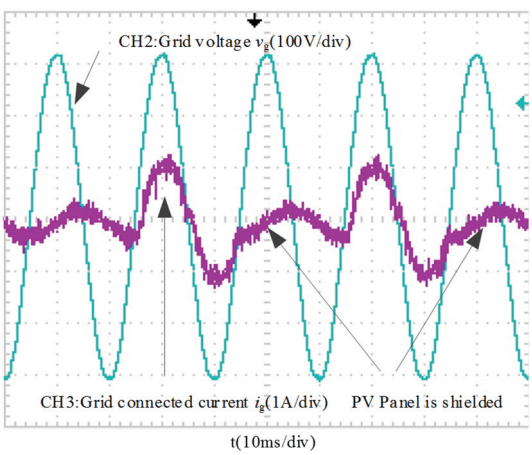


Fig. 12. Occlusion experiment of a photovoltaic module.

that the presented sliding mode controller can be applied to the CIDBI and that it can transfer energy from the dc side to the mains grid with high quality.

Fig. 10 shows waveforms of the grid voltage and grid-connected current when the prototype starts. As can be seen from this figure, when the prototype starts grid-connected power generation, the current $i_g$ begins to gradually increase. After a period of time, the current reaches its maximum value and constant. Channel 1 of Fig. 11 shows a voltage waveform of capacitor $C_2$ in the right circuit of the CIDBI, and channel 2 shows a driving waveform of the switch $T_1$. Channel 3 of Fig. 12 shows a grid-connected current waveform ($i_g$) when the photovoltaic panel is shielded or not. Channel 2 of Fig. 12 shows the grid voltage. From the above experimental waveforms, it can be seen that using the two sliding mode controllers proposed in this paper can yield both the stability of micro-inverters based on the CIDBI architecture, and a fast dynamic response speed.

## V. Conclusions

A CIDBI can be used to generate an ac output voltage that is larger than the dc input voltage and to transfer energy from a PV array or dc energy storage device to a grid with only one power processing stage. Aiming at the problem of it being difficult to design the parameters of the traditional regulators for the high-order systems of CIDBI circuits, different sliding-mode controllers are proposed in this paper for the right-side converter and the left-side converter with different switching schemes. In addition, the SMCs can track the time-varying reference functions very well. These functions are only defined for two output variables. The other secondary signals are obtained after high-pass filtering. The use of such SMCs can achieve remarkable overall performance improvements of the system.

## Acknowledgment

This paper was supported in part by the National Natural Science Foundation of China under Grant 61873346, in part by the Science and Technology Cooperation Fund of Yangzhou City Hall project under Grant YZ2018136, in part by the Intelligent Energy Internet Research Institute Joint Fund of State Grid Yangzhou Power Supply Company and Yangzhou University under Grant SGTYHT/17-JS-202, and in part by the Open Project Fund of Yangzhou University Jiangdu Institute of High-end Equipment Engineering Technology under Grant YDJD201902.

## References

[1] Y. Fang and X. Ma, "A novel PV micro inverter with coupled inductors and double-boost topology," *IEEE Trans. Power Electron.*, Vol. 25, No. 12, pp. 3139-3147, Dec. 2010.

[2] K. Zhao, T. Yin, C. Zhang, J. He, X. Li, Y. Chen, R. Zhou, and A. Leng, "Robust model-free nonsingular terminal sliding mode control for PMSM demagnetization fault," *IEEE Acces*s, pp. 15737-15748, 2019.

[3] Y. Yueneng and Y. Ye, "Back stepping sliding mode control for uncertain strict-feedback nonlinear systems using neural-network-based adaptive gain scheduling," *J. Syst. Eng. Electron.*, Vol. 29, No. 3, pp. 580-586, Mar. 2018.

[4] A. Musa, L. R. Sabug, and A. Monti, "Robust predictive sliding mode control for multiterminal HVDC grids," *IEEE Trans. Power Del.*, Vol. 33, No. 4, pp. 1545-1555, Aug. 2018.

[5] M. B. Delghavi and A. Yazdani, "Sliding-mode control of AC voltages and currents of dispatchable distributed energy resources in master-slave-organized inverter-based microgrids," *IEEE Trans. Smart Grid*, Vol. 10, No. 1, pp. 980-991, Oct. 2019.

[6] W. Na, R. Kohl, and W. Chung, "Sliding mode control of a power factor corrected converter for Plug-In Hybrid Electric Vehicles," *38th Annual Conference on IEEE Industrial Electronics Society (IECON)*, pp. 763-767, 2012.

[7] R. Wai and L. Z. Shin, "Total sliding-mode voltage tracking control for DC-DC boost converter," *6th IEEE Conference on Industrial Electronics and Applications (ICIEA)*, pp. 2676-2681, 2011.

[8] R. J. Wai and L. C. Shih, "Design of voltage tracking control for DC–DC boost converter via total sliding-mode technique," *IEEE Trans. Ind. Electron.*, Vol. 58, No. 6, pp. 2502-2511, Jun. 2010.

[9] M. Salimi, J. Soltani, A. Zakipour, and V. Hajbani, "Sliding mode control of the DC-DC flyback converter with zero steady-state error," *4th Power Electronics, Drive Systems and Technologies Conference (PEDSTC)*, pp. 158-163. 2013.

[10] M. Cucuzzella, G. P. Incremona, and A. Ferrara, "Decentralized sliding mode control of islanded AC microgrids with arbitrary topology," *IEEE Trans. Ind. Electron.*, Vol. 64, No. 8, pp. 6706-6713, Aug. 2017.

[11] R. Ling, Y. Dong, M. Wu, and Y. Chai, "Decentralized sliding mode control of WG/PV/FC micro grids under unbalanced and nonlinear load conditions for on- and off-grid modes," *IEEE Syst. J.*, Vol. 12, No. 4, pp. 3108-3119, Dec. 2018.

[12] H. Ma, Q. W. Liu, and J. Guo, "A sliding-mode control scheme for LLC resonant DC/DC converter with fast transient response," *38th Annual Conference on IEEE Industrial Electronics Society (IECON)*, pp. 162-167, 2012.

[13] M. A. M. Cheema, J. E. Fletcher, M. Farshadnia, and M. F. Rahman, "Sliding mode based combined speed and direct thrust force control of linear permanent magnet synchronous motors with first-order plus integral sliding condition," *IEEE Trans. Power Electron.*, Vol. 34, No. 3, pp. 2526-2538, Mar. 2019.

[14] J Monteiro, J. F. Silva, S. F. Pinto, and J. Palma, "Linear and sliding-mode control design for matrix converter-based unified power flow controllers," *IEEE Trans. Power Electron.*, Vol. 29, No. 7, pp. 3357-3367, Jul. 2014.

[15] B. Labbe, B. Allard, L. S. Xuefang, and D. Chesneau, "An integrated sliding-mode buck converter with switching frequency control for battery-powered applications," *IEEE Trans. Power Electron.*, Vol.28, No. 9, pp. 4318-4326, Sep. 2013.

[16] G. H. Sun, Z. Q. Ma, and J. Y. Yu, "Discrete-time fractional order terminal sliding mode tracking control for linear motor," *IEEE Trans. Ind. Electron.*, Vol. 65, No. 4, pp. 3386-3394, Apr. 2018.

[17] L. J. Zheng, F. Y. Jiang, J. C. Song, Y. G. Gao, and M. Tian, "A discrete-time repetitive sliding mode control for voltage source inverters," *IEEE J. Emerg. Sel. Topics Power Electron.*, Vol. 6, No. 3, pp. 1553-1566, Sep. 2018.

[18] R. Haroun, A. Cid-Pastor, A. El Aroudi, and L. Martinez-Salamero, "Synthesis of canonical elements for power processing in DC distribution systems using cascaded converters and sliding-mode control," *IEEE Trans. Power Electron.*, Vol. 29, No. 3, pp. 1366-1381, Mar. 2014.

[19] P. K. Singh, Y. V. Hote, and M. M. Garg, "Comments on PI and sliding mode control of a cuk converter," *IEEE Trans. Power Electron.*, Vol. 29, No. 3, pp. 1551-1552, Mar. 2014.

[20] Y. D. Lv, H. S. Yu, and X. D. Liu, "Switching control of sliding mode and passive control for DC-Link voltage of isolated shoot-through Z-source inverter," *Chinese Automation Congress (CAC)*, pp. 2687-2692, 2018.

[21] G. P. Incremona, M. Rubagotti, and A. Ferrara, "Sliding mode control of constrained nonlinear systems," *IEEE Trans. Autom. Contr.*, Vol. 62, No. 6, pp. 2965-2972, Jun. 2017.

[22] J. Song, Z. T. Liu, and H. Y. Su, "A second-order sliding mode control design for bidirectional DCDC converter," *36th Chinese Control Conference (CCC)*, pp. 9181-9186, 2017.

[23] H. Liu and D. W. Qian, "Sliding-mode-based disturbance rejection control of nonlinear power systems with renewable sources," *International Conference on Advanced Mechatronic Systems (ICAMechS)*, pp. 238-243, 2015.

[24] X. C. Meng, H. S. Yu, and X. D. Liu, "Adaptive back stepping speed control and sliding mode current regulation of permanent magnet synchronous motor," *Chinese Control and Decision Conference (CCDC)*, pp. 4025-4029, 2018.

[25] H. P. Ren and R. Zhou, "Fuzzy sliding mode tracking control for DC motor servo system without uncertainty information," *12th IEEE Conference on Industrial Electronics and Applications (ICIEA)*, pp. 1511-1515, 2017.

[26] G. P. Incremona, M. Rubagotti and A. Ferrara, "Sliding mode control of constrained nonlinear systems," *IEEE Trans. Autom. Contr.*, Vol. 62, No. 6, pp. 2965-2972, Jun. 2017.

[27] S. K. Pandey, S. L. Patil, and S. B. Phadke, "Comment on PWM-based adaptive sliding-mode control for Boost DC–DC converters," *IEEE Trans. Ind. Electron.,* Vol. 65, No. 6, pp. 5078-5080, Jun. 2018.

**Yu Fang** was born in Jiangsu Province, China, in 1972. He received his B.S. degree in Electrical Engineering and Automation from the Wuhan University of Technology, Wuhan, China, in 1995; and his M.S. and Ph.D. degrees in Power Electronics and Power Drives from the Nanjing University of Aeronautics and Astronautics (NUAA), Nanjing, China, in 2004 and 2008, respectively. He worked in the Post-Doctoral Workstation of Southeast University (SU), Nanjing, China; was an Academic Visitor at the University of Nottingham, Nottingham, ENG, UK; and is presently working as a Professor in the College of Information Engineering, Yangzhou University, Yangzhou, China. Dr. Fang has authored more than 80 technical papers published in journals and conference proceedings. His current research interests include modeling, digital control of switching power converters, bidirectional energy converters applied to new energy grid-connected generation and energy internet.

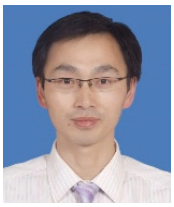

**Songyin Cao** was born in Jiangsu Province, China, in 1982. He received his M.S. degree from the College of Information Engineering, Yangzhou University (YZU), Yangzhou, China, in 2006; and his Ph.D. degree from the School of Automation, Southeast University, Nanjing, China, in 2011. Since 2010, he has been with the Faculty of Automation, YZU, where he is presently working as an Associate Professor in the College of Information Engineering. From 2012 to 2015, he was a Post-Doctoral Fellow at Beihang University, Beijing, China. From 2014 to 2015, he was an Academic Visitor at Loughborough University, Loughborough, ENG, UK. He has published one book and authored more than 40 technical papers published in journals and conference proceedings. His current research interests include fault tolerant control and inertial navigation systems.

**Pat Wheeler** received his B.S. [Hons] degree, and his Ph.D. degree in Electrical Engineering for his work on Matrix Converters from the University of Bristol, Bristol, ENG, UK, in 1990 and 1994, respectively. In 1993, he moved to the University of Nottingham, Nottingham, ENG, UK, and worked as a Research Assistant in the Department of Electrical and Electronic Engineering. In 1996, he became a Lecturer in the Power Electronics, Machines and Control Group at the University of Nottingham, where he has been a Full Professor since 2008. He is presently serving as the Head of the Department of Electrical and Electronic Engineering at the University of Nottingham. He is an IEEE PELs 'Member at Large' and an IEEE PELs Distinguished Lecturer. He has published over 400 academic papers in leading international journals and conference proceedings.